Supporting Information

# Accurate Fabrication and Orientation of Electron Acceptor and Donor Active Sites for Enhancing Photocatalytic Overall Water Splitting

Yan Wu,[a†] Qingqing Chen,[a†] Jiaping Liu,[a] Kai Fang,[a] Man Zhang,[b] Tao Jing[c,*] Zhujie Li,[b*] and Gang Wang[a*]

[a]Key Laboratory of Functional Molecular Solids, Ministry of Education, College of Chemistry and Materials Science, Anhui Normal University, Wuhu, 241002, P. R. China. E-mail: GangWang@ahnu.edu.cn

[b]Advanced Technology Research Institute, Beijing Institute of Technology, Jinan, 250300, P. R. China. E-mail: zhujieli89@163.com

[c]College of Science, Kaili University, Kaili, 556011, P. R. China.

[†]The authors contributed equally to this work.

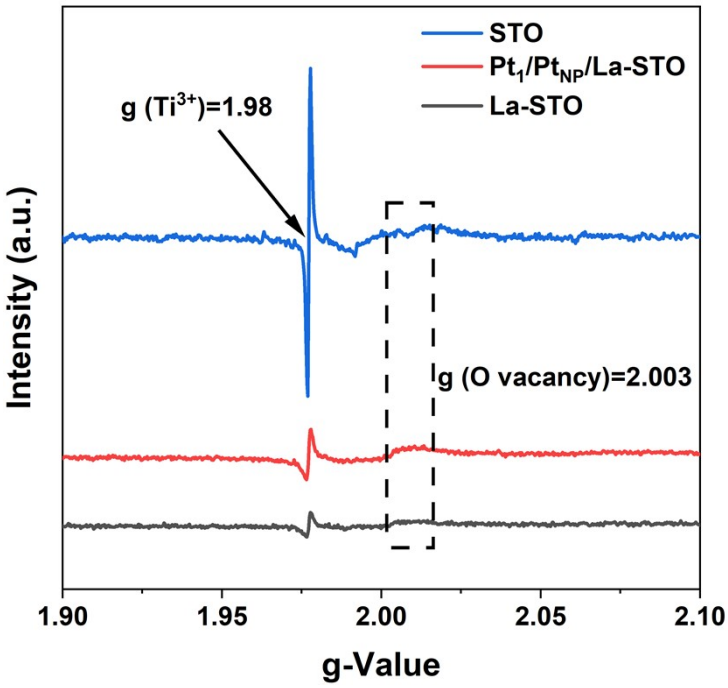


**Fig. S1.** EPR results of STO, La-STO and $Pt_1/Pt_{NP}$/La-STO. A large number of $Ti^{3+}$ defect existed in the pure STO. After La doped, the $La^{3+}$ ions were conducive to decrease the $Ti^{3+}$ defect content, which was beneficial for improving the quality of STO crystal.

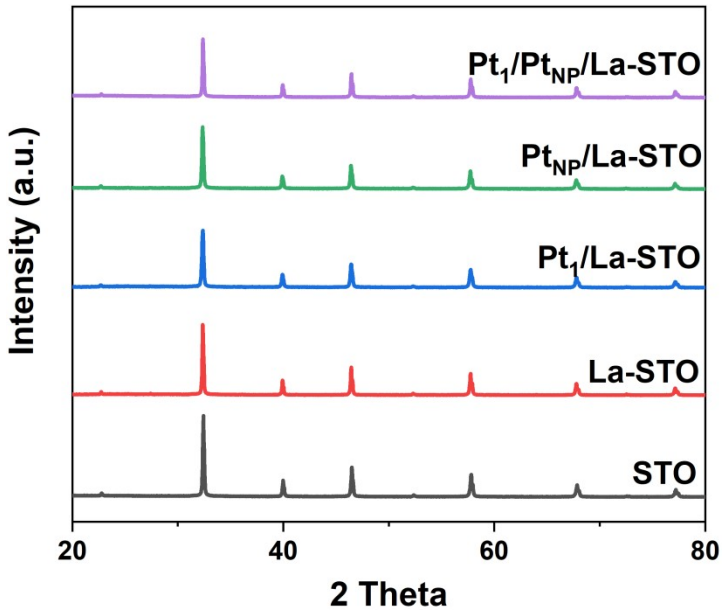


**Fig. S2.** X-ray diffraction patterns of STO, La-STO, $Pt_1$/La-STO, $Pt_{NP}$/La-STO and $Pt_1/Pt_{NP}$/La-STO.

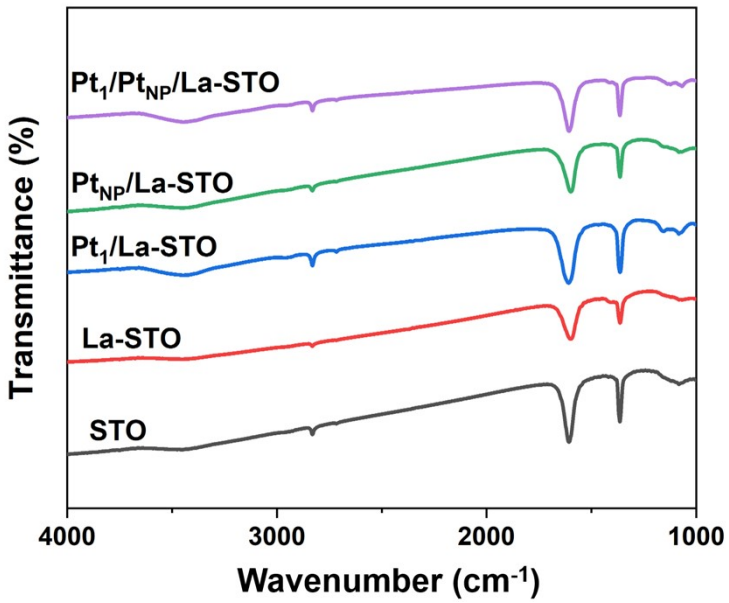


**Fig. S3.** Fourier transforms infrared spectroscopy (FT-IR) spectra in the zone of 4000-1000 $cm^{-1}$.

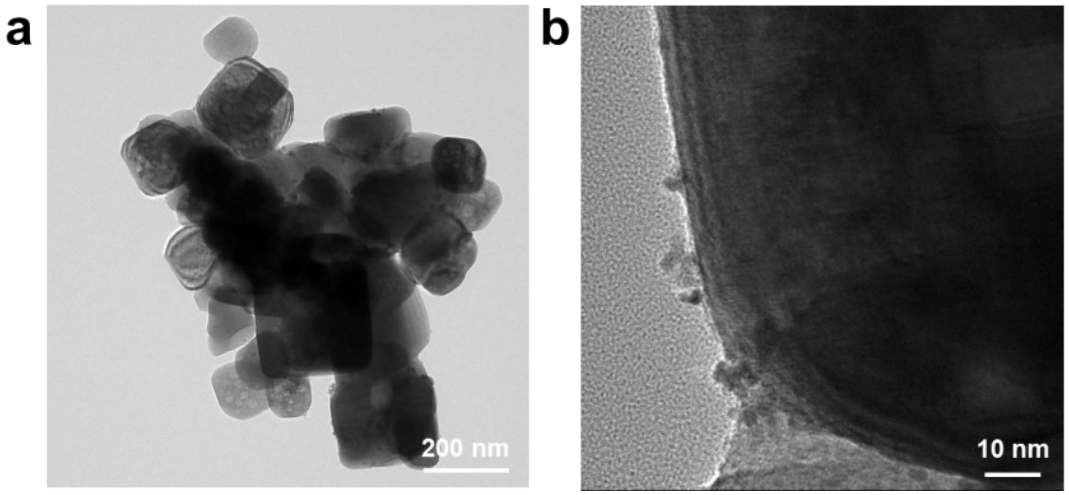


**Fig. S4.** Transmission electron microscopy (TEM) images of $Pt_1/Pt_{NP}$/La-STO.

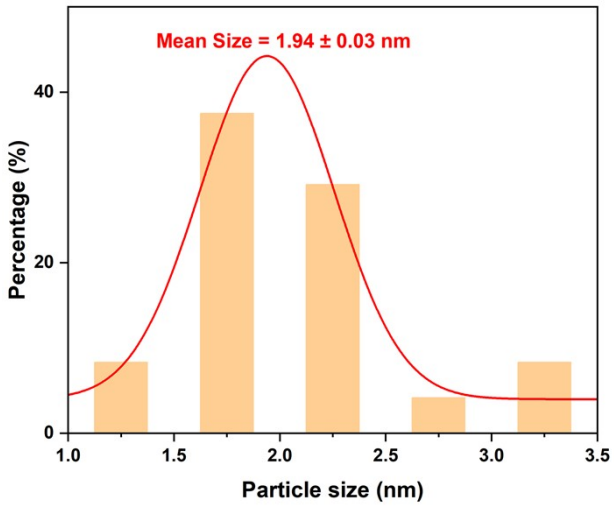


**Fig. S5.** The size distribution histograms of $Pt_{NP}$ (scale bar: 50 nm).

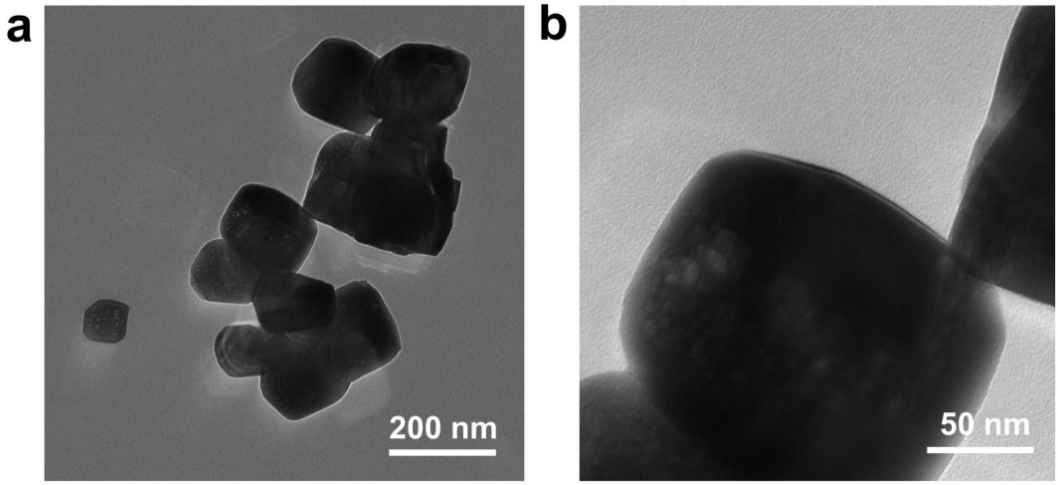


**Fig. S6.** TEM images of STO.

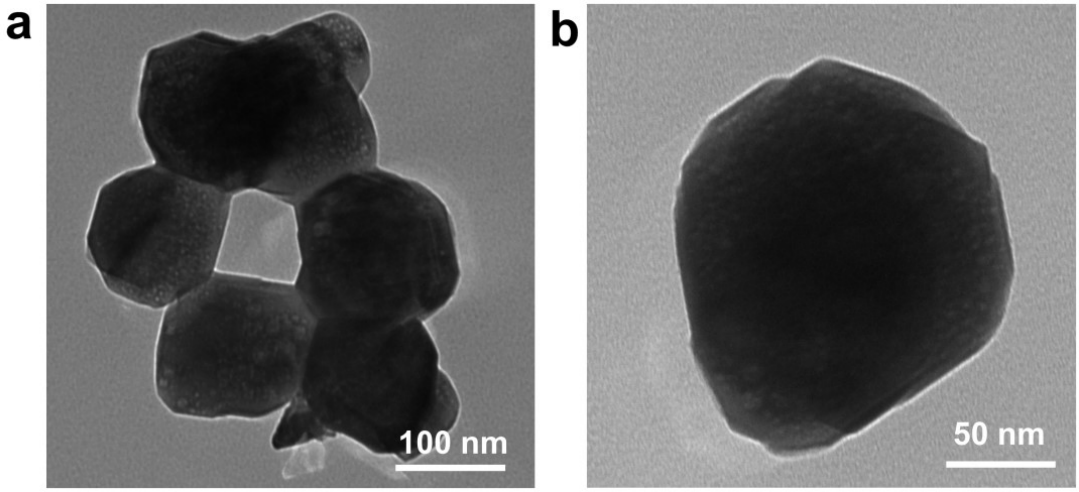


**Fig. S7.** TEM images of La-STO.

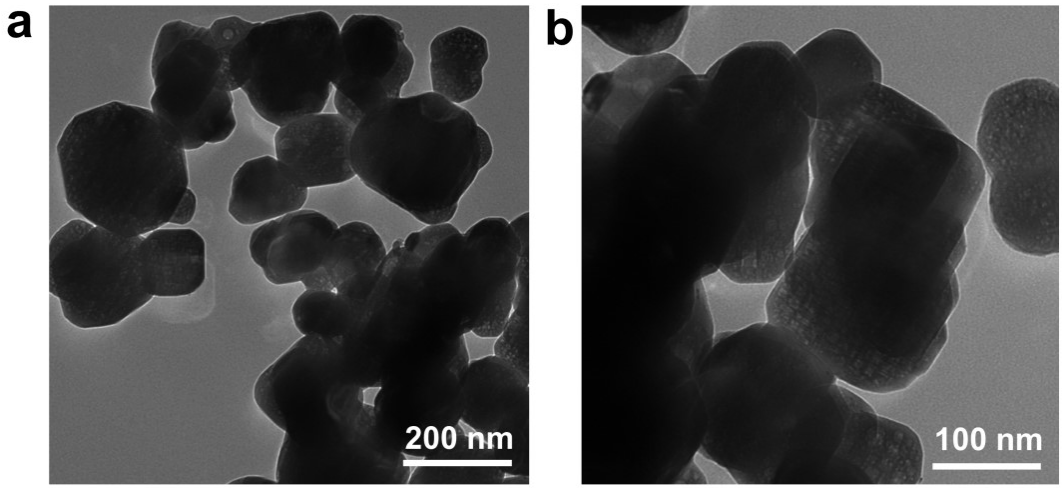


**Fig. S8.** TEM images of $Pt_1$/La-STO.

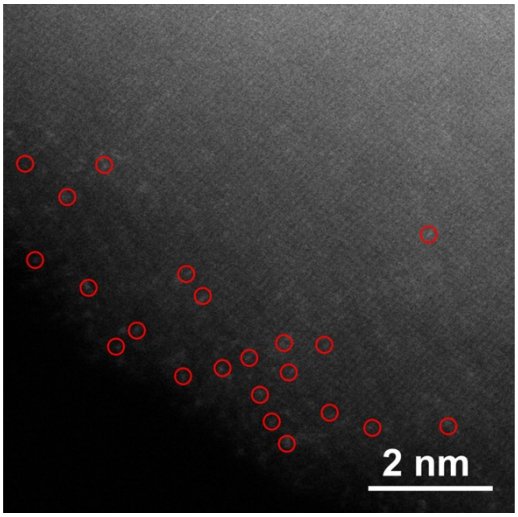


**Fig. S9.** HAADF-STEM image of $Pt_1$/La-STO.

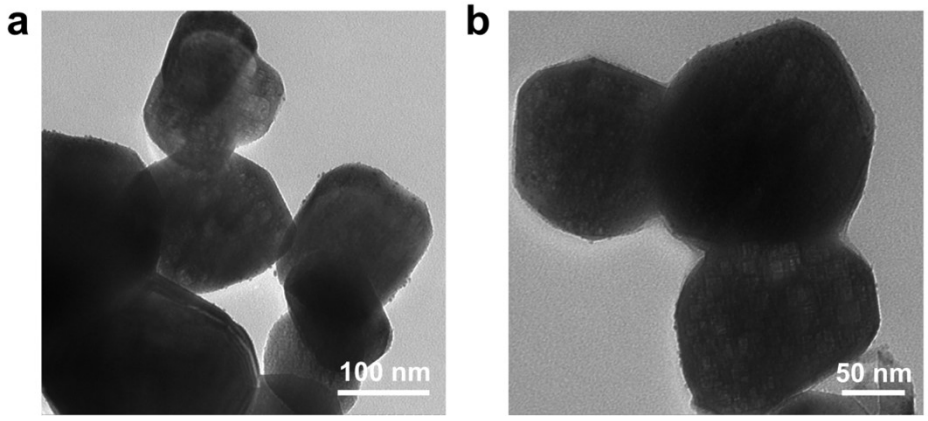


**Fig. S10.** TEM images of $Pt_{NP}$/La-STO.

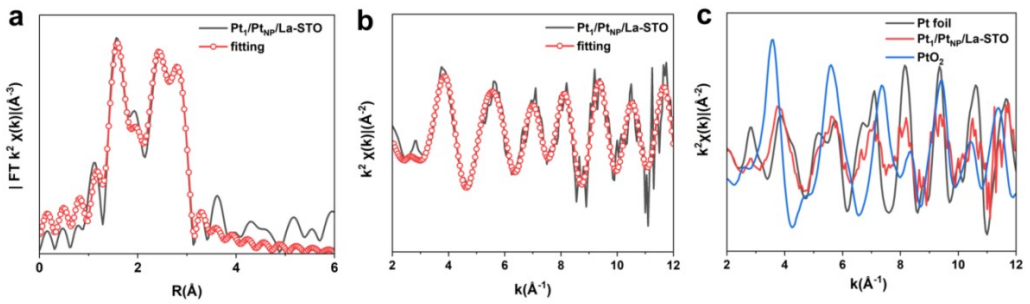


**Fig. S11.** EXAFS (a) R space and (b) k-space fitting curves of $Pt_1/Pt_{NP}$/La-STO. FT-EXAFS spectra at (c) k-space of $Pt_1/Pt_{NP}$/La-STO, Pt foil and $PtO_2$.

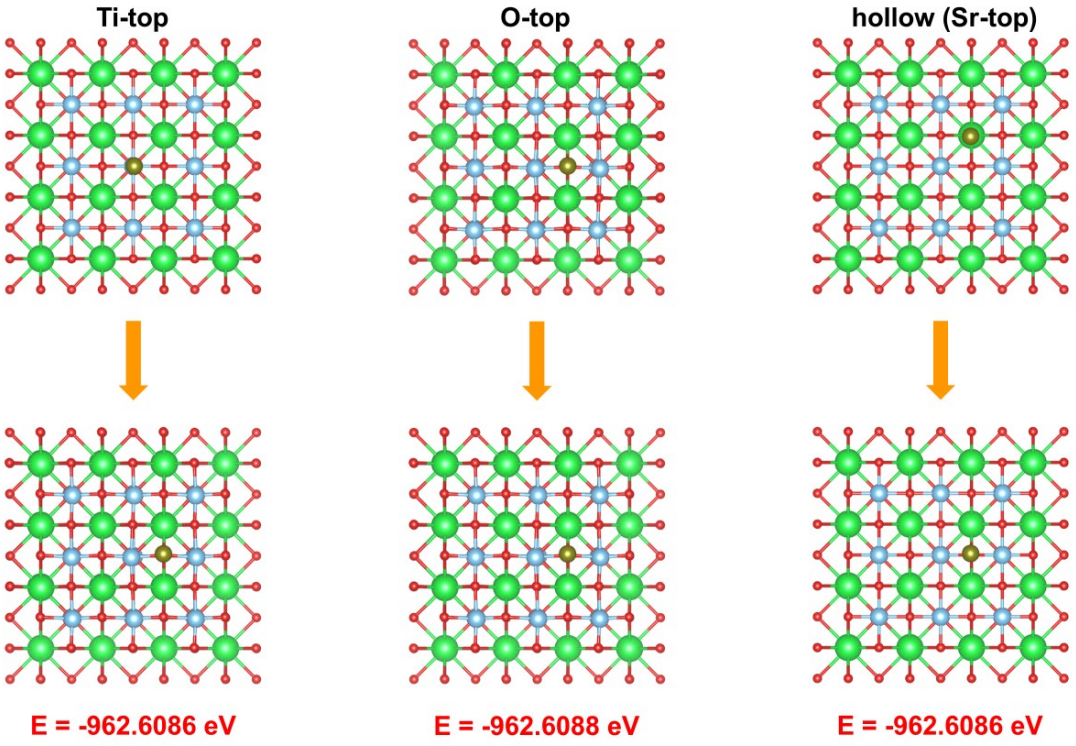


**Fig. S12.** The upper and lower panels show the three different initial configurations of Pt single atom on La-STO and their corresponding optimized structures, respectively. As shown in the lower panels, all the three configurations become the O-top structure, which confirms the most stable position for single atom Pt. The green, blue, red and brown balls are represented as Sr, Ti, O and Pt atoms, respectively.

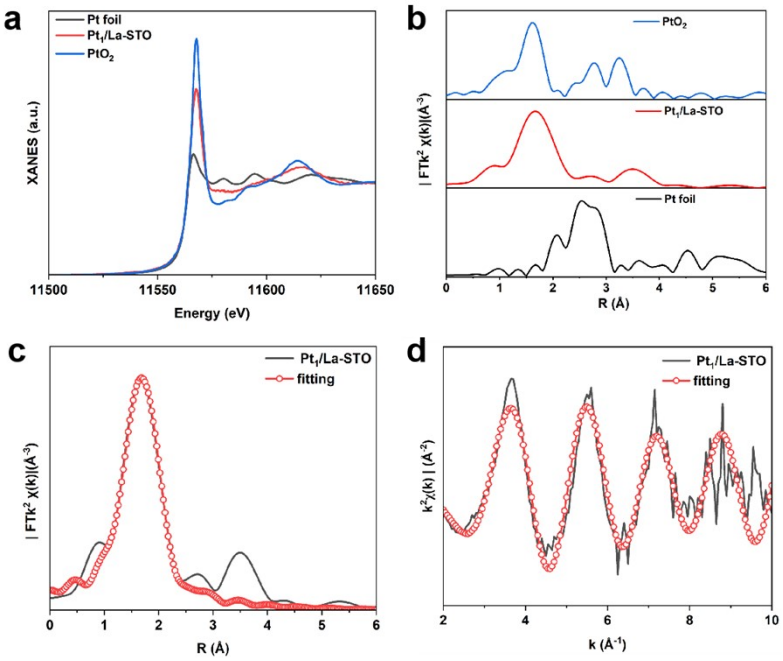


**Fig. S13.** (a) Pt $L_3$-edge XANES spectra of $Pt_1$/La-STO, Pt foil and $PtO_2$. (b) FT-EXAFS spectra at R space of $Pt_1$/La-STO. (c) R-space fitting results of $Pt_1$/La-STO. (d) k-space fitting results of $Pt_1$/La-STO.

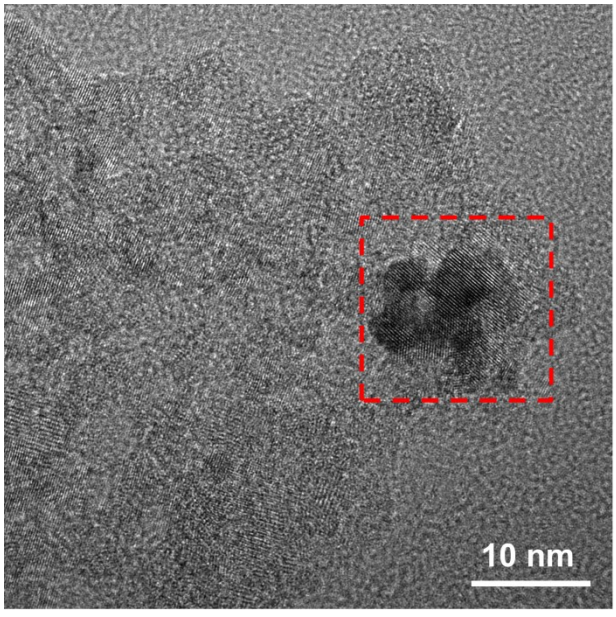


**Fig. S14.** HRTEM image of $Pt_1/Pt_{NP}/TiO_2$ (red box is $Pt_{NP}$).

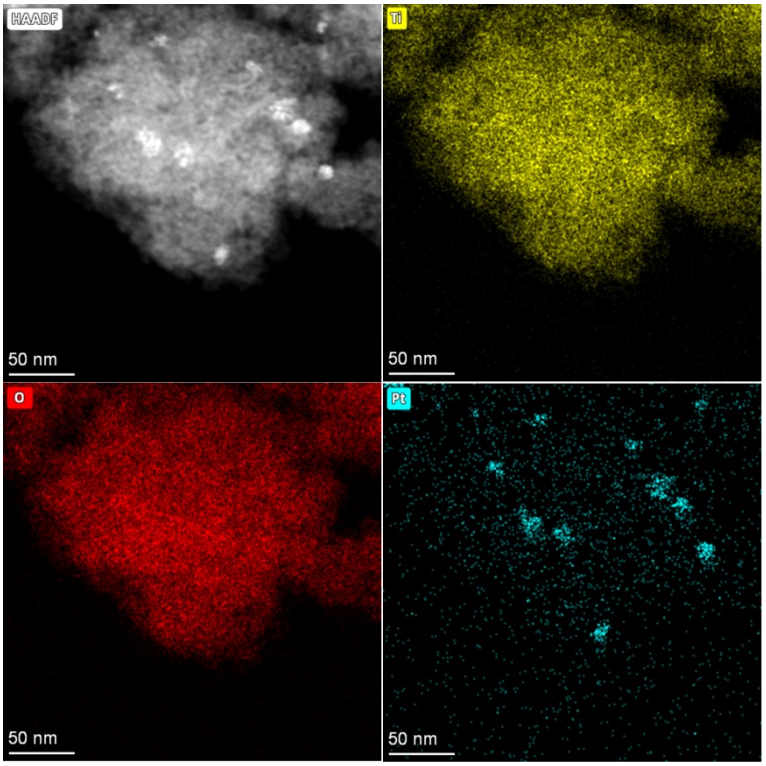


**Fig. S15.** EDS mapping images of $Pt_1/Pt_{NP}/TiO_2$.

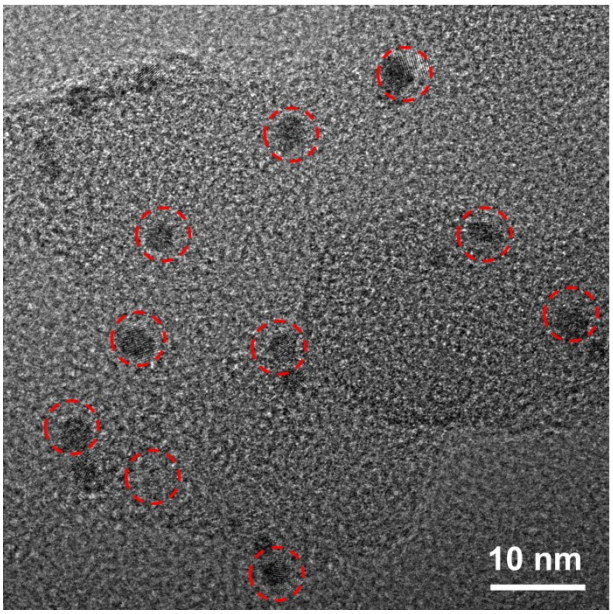


**Fig. S16.** HRTEM image of $Pt_1/Pt_{NP}/g\text{-}C_3N_4$ (red box is $Pt_{NP}$).

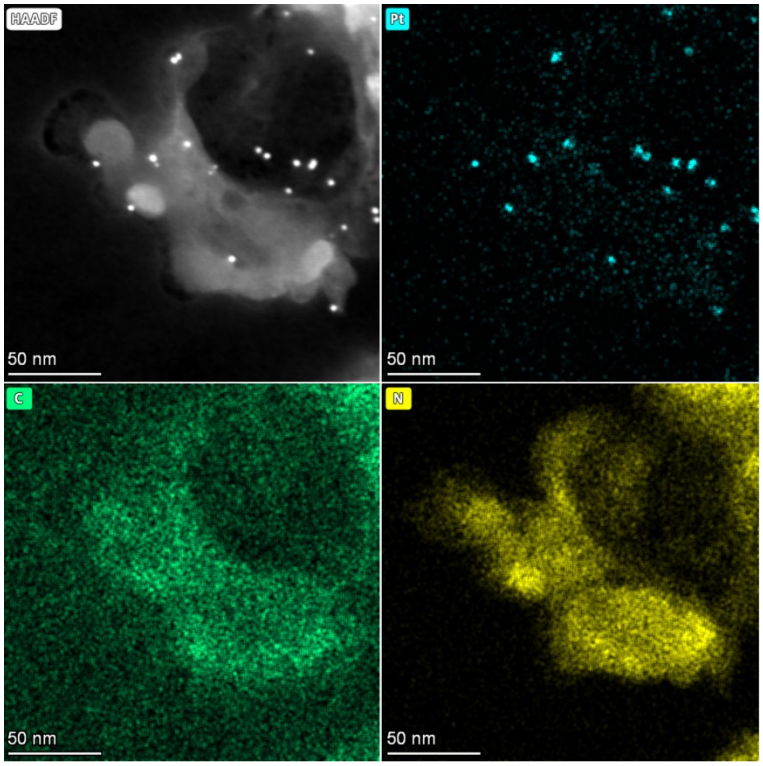


**Fig. S17.** EDS mapping images of $Pt_1/Pt_{NP}/g\text{-}C_3N_4$.

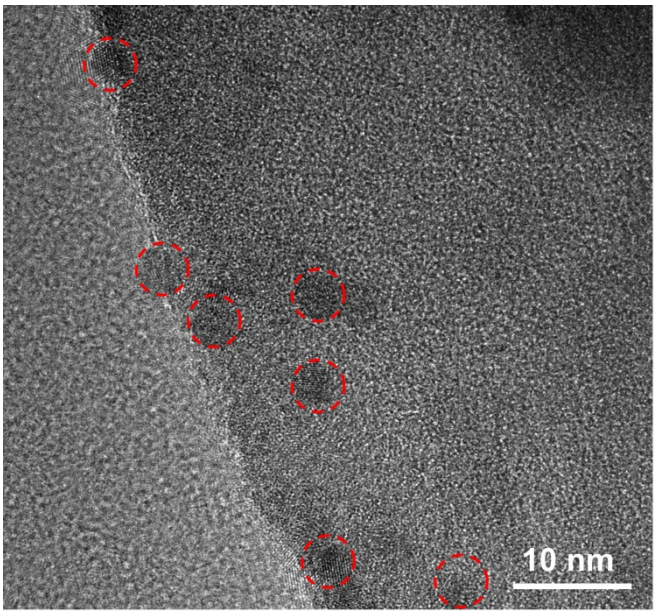


**Fig. S18.** HRTEM image of $Pt_1/Pt_{NP}$/MIL-125 (red box is $Pt_{NP}$).

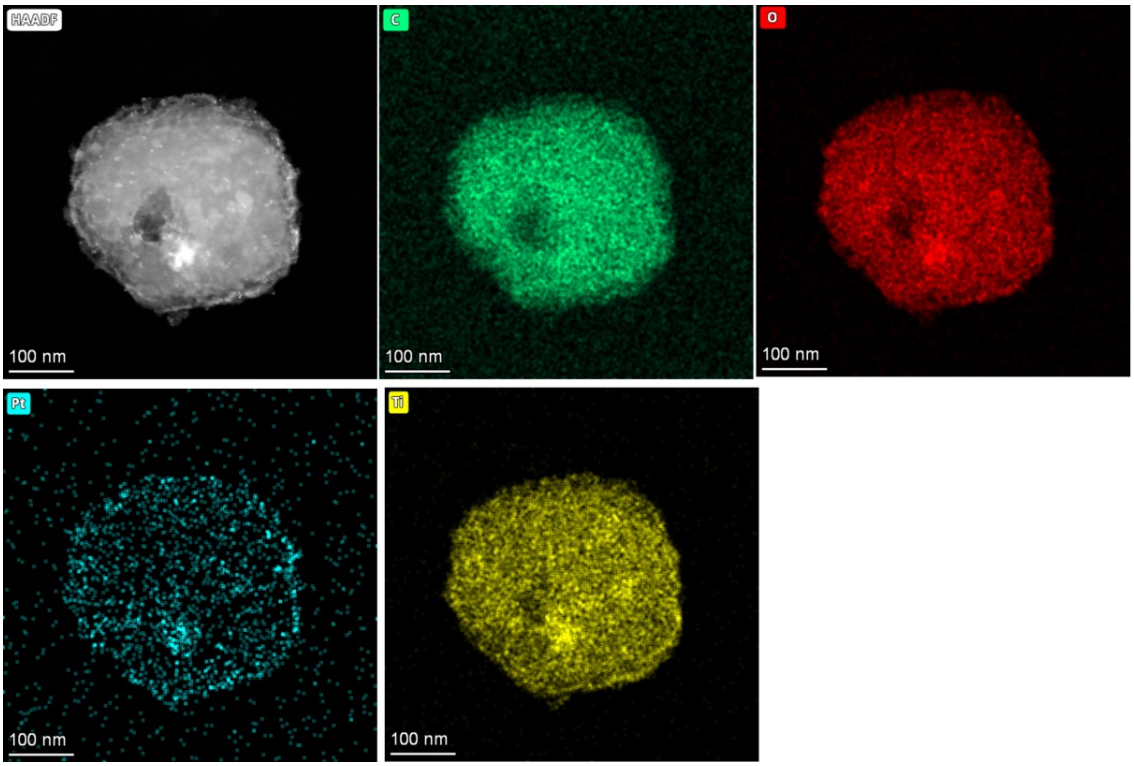


**Fig. S19.** EDS mapping images of $Pt_1/Pt_{NP}$/MIL-125.

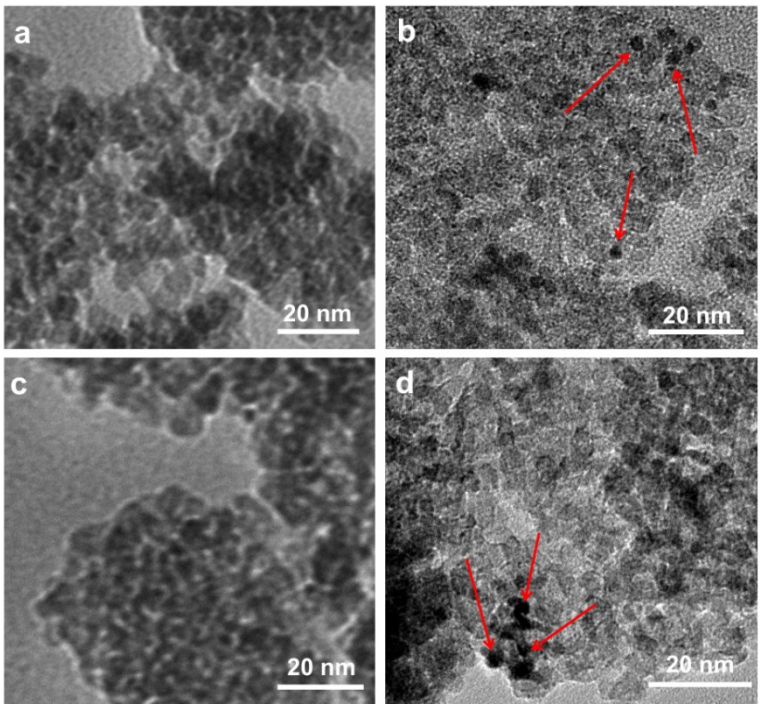


**Fig. S20.** TEM images of (a) $TiO_2$, (b) $Pt_{NP}/TiO_2$, (c) $Pt_1/TiO_2$ and (d) $Pt_1/Pt_{NP}/TiO_2$.

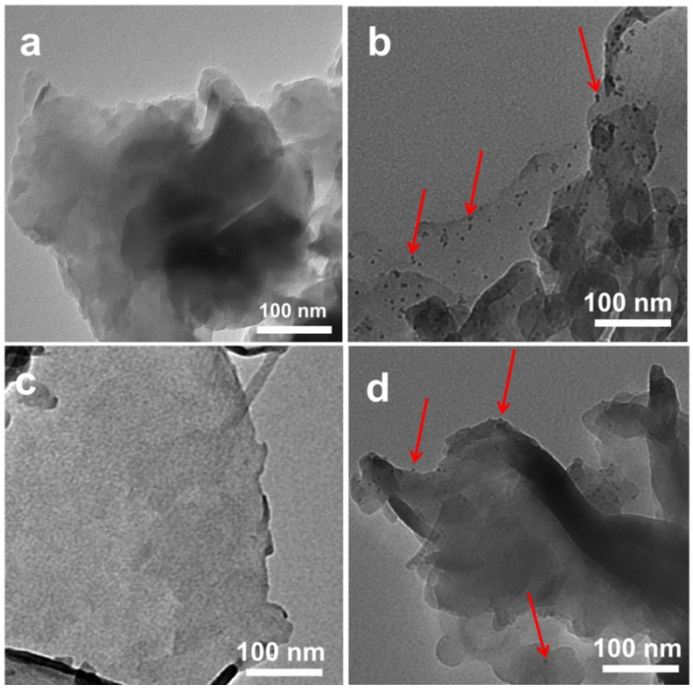


**Fig. S21.** TEM image of (a) g-$C_3N_4$, (b) $Pt_{NP}$/g-$C_3N_4$, (c) $Pt_1$/g-$C_3N_4$ and (d) $Pt_1$/$Pt_{NP}$/g-$C_3N_4$.

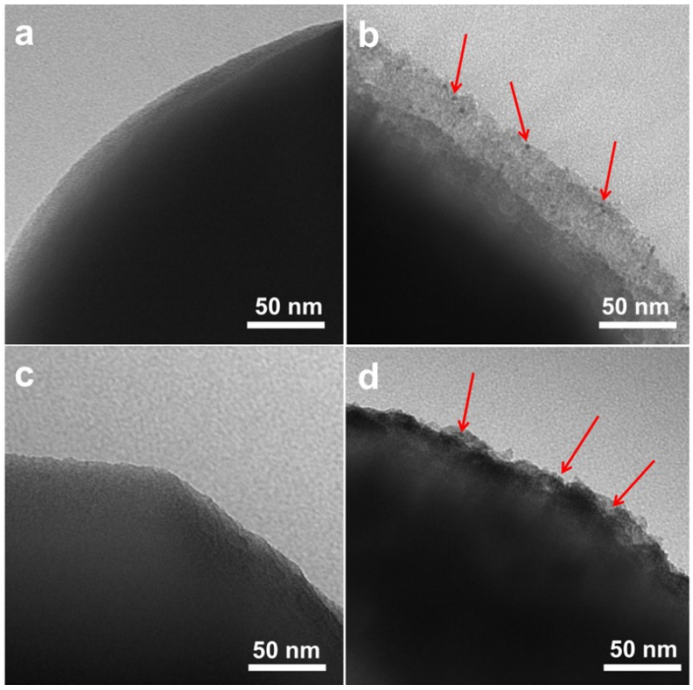


**Fig. S22.** TEM image of (a) MIL-125, (b) $Pt_{NP}$/MIL-125, (c) $Pt_1$/MIL-125 and (d) $Pt_1$/$Pt_{NP}$/MIL-125.

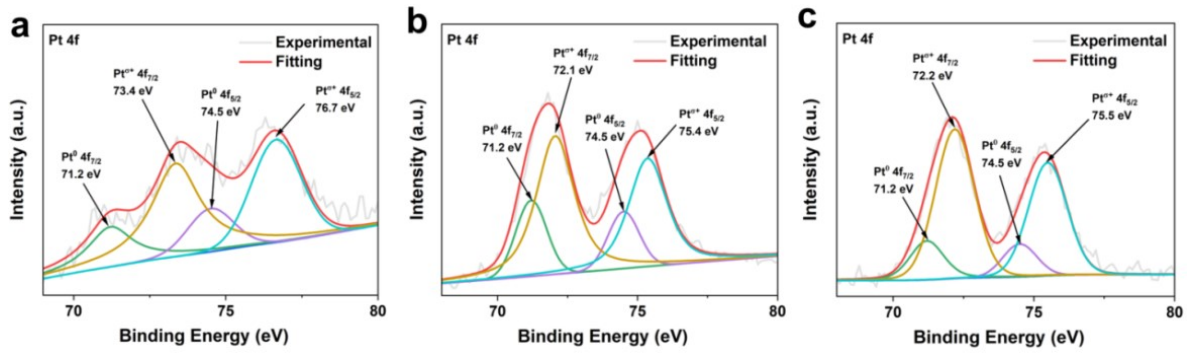


**Fig. S23.** The XPS spectra of Pt species in (a) $Pt_1/Pt_{NP}/TiO_2$, (b) $Pt_1/Pt_{NP}$/MIL-125, (c) $Pt_1/Pt_{NP}/g\text{-}C_3N_4$.

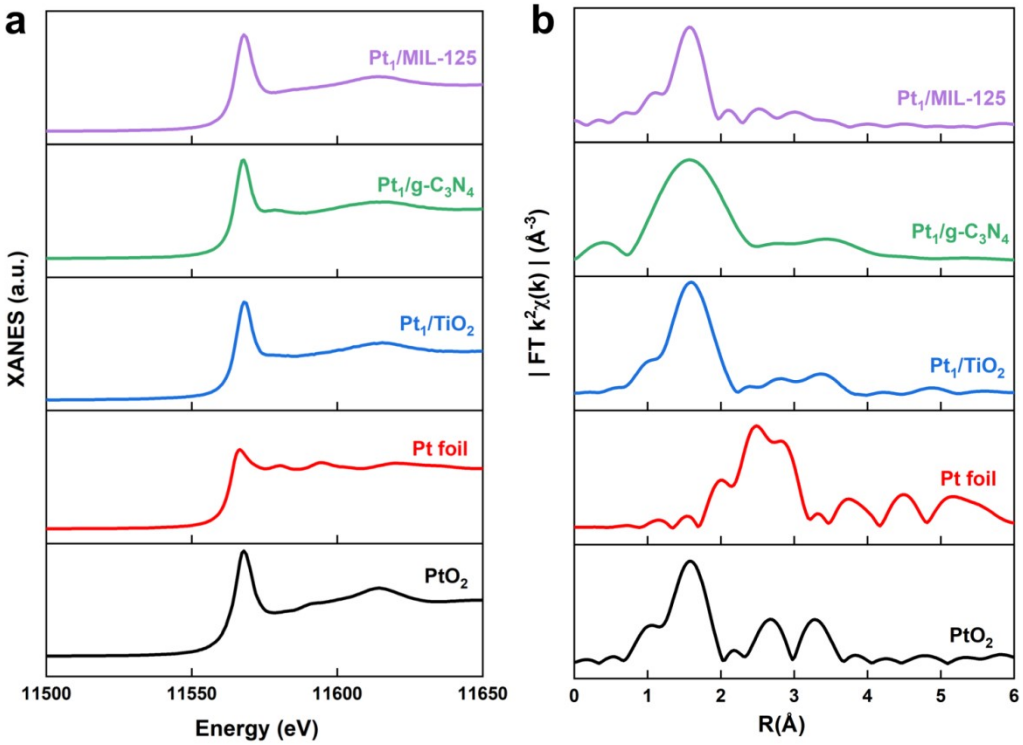


**Fig. S24.** (a) Pt $L_3$-edge XANES spectra of $Pt_1$/MIL-125, $Pt_1/g\text{-}C_3N_4$, $Pt_1/TiO_2$, Pt foil and $PtO_2$. (b) FT-EXAFS spectra at R space of $Pt_1$/MIL-125, $Pt_1/g\text{-}C_3N_4$, $Pt_1/TiO_2$, Pt foil and $PtO_2$. The above results imply the single atom of Pt anchored on these supports.

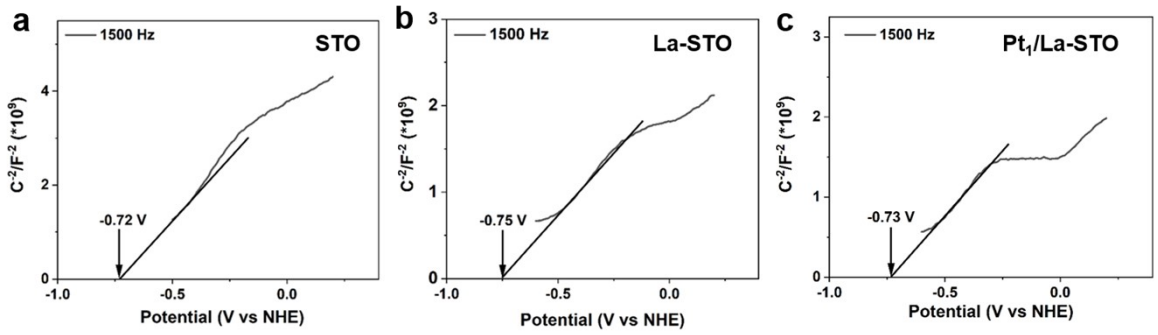


**Fig. S25.** Mott-Schottky (M-S) plots of the (a) STO, (b) La-STO, (c) $Pt_1$/La-STO. The flat band potentials have been transferred to the values under pH=0 by using the equations of $E_{Ag/AgCl}=E_{RHE}-0.059pH-0.197$ and $E_{NHE}=E_{RHE}-0.059pH$. The flat band potential obtained by the M-S plots is approximately 0.1 V below their conductor band positions for n-type semiconductor. The $E_{CBM}$ are about -0.82, -0.85, -0.83 V vs NHE (pH=0) for STO, La-STO and $Pt_1$/La-STO respectively.

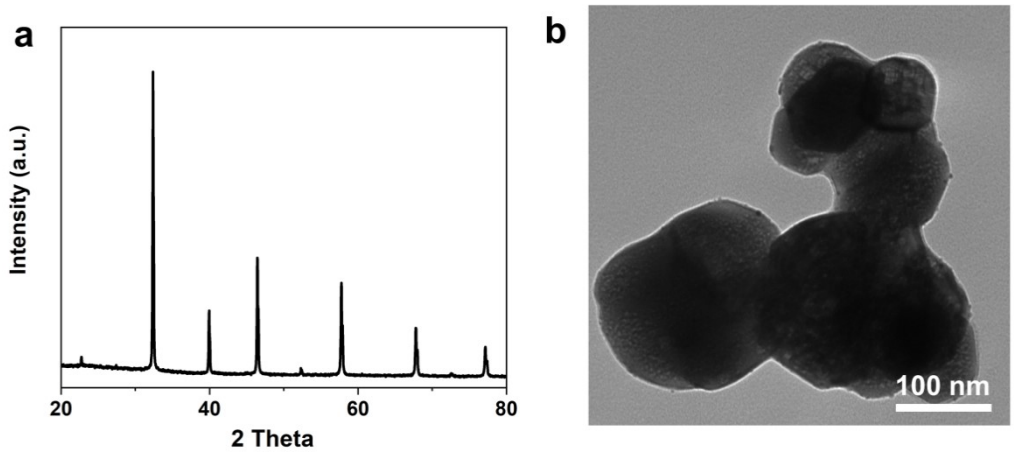


**Fig. S26.** The crystal structure and morphology of the used $Pt_1/Pt_{NP}$/La-STO. (a) XRD pattern. (b) TEM image.

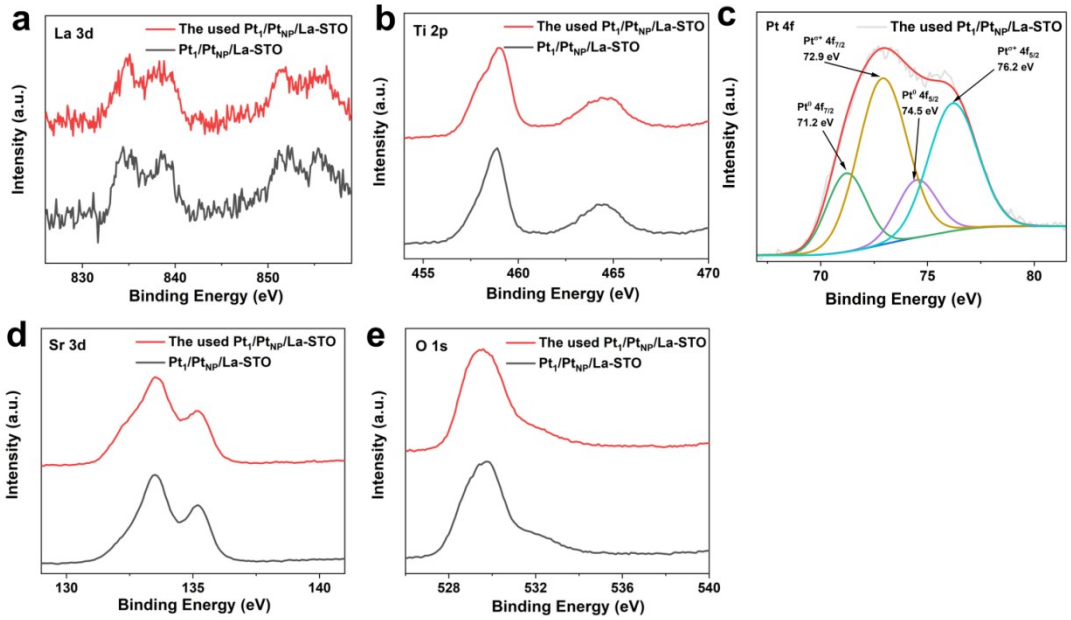


**Fig. S27.** The element chemical states of the used $Pt_1/Pt_{NP}$/La-STO.

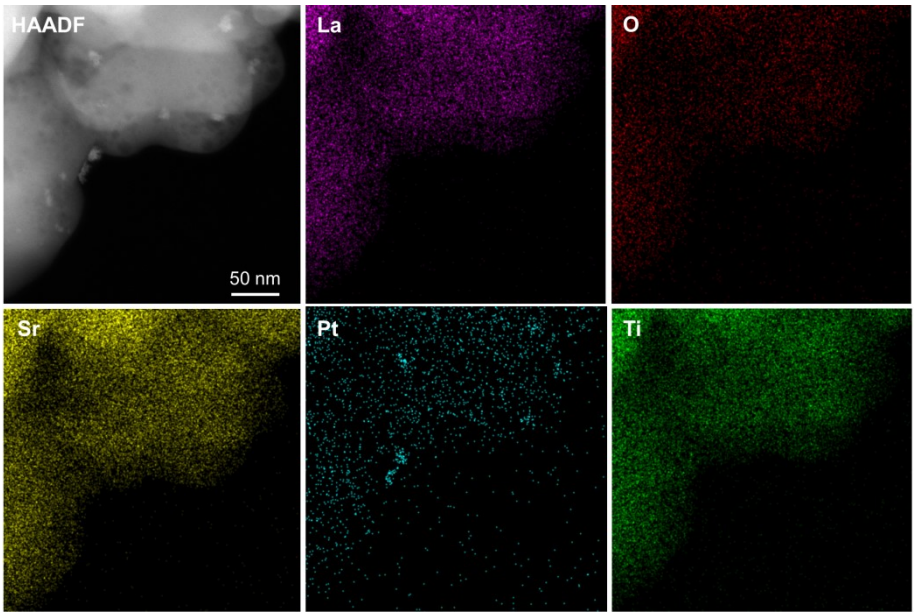


**Fig. S28.** Elemental mapping images of $Pt_1/Pt_{NP}$/La-STO after stability test photocatalytic overall water splitting under light irradiation.

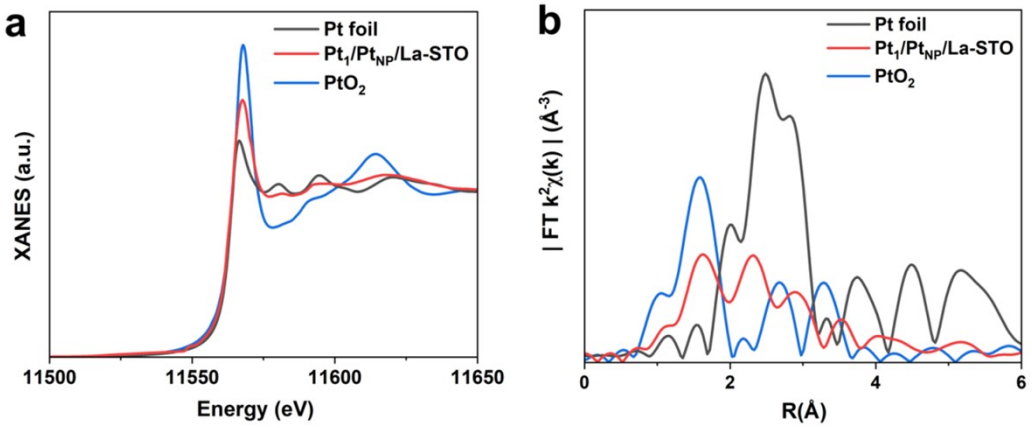


**Fig. S29.** (a) Pt $L_3$-edge XANES spectra of the used $Pt_1/Pt_{NP}$/La-STO, Pt foil and $PtO_2$. (b) FT-EXAFS spectra at R space of the used $Pt_1/Pt_{NP}$/La-STO, Pt foil and $PtO_2$.

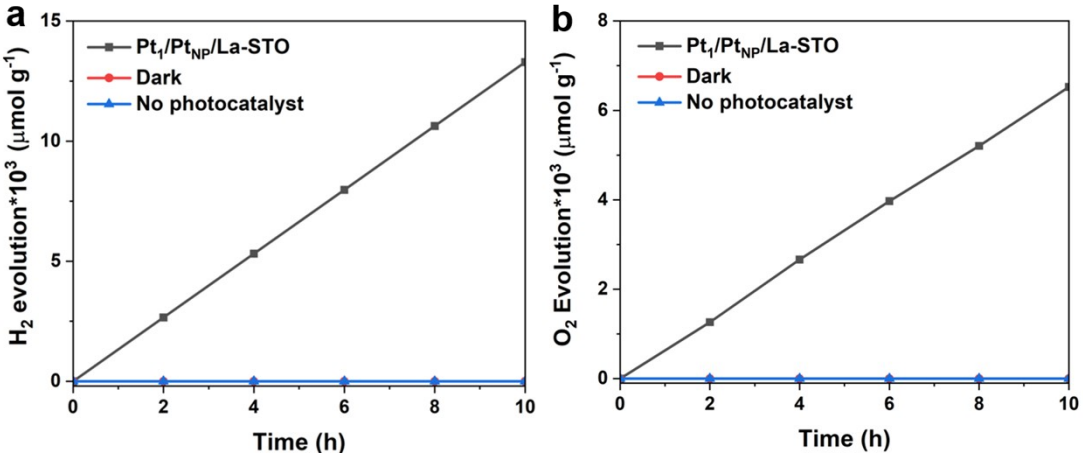


**Fig. S30.** The control experiments of photocatalytic OWS upon $Pt_1/Pt_{NP}$/La-STO at different condition after 10 hours light irradiation.

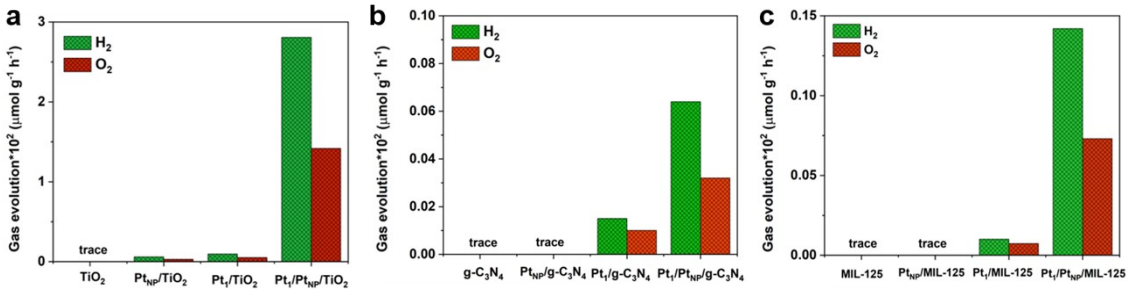


**Fig. S31.** The photocatalytic OWS activities upon $Pt_1/Pt_{NP}/TiO_2$, $Pt_1/Pt_{NP}/g\text{-}C_3N_4$ and $Pt_1/Pt_{NP}$/MIL-125 their corresponding control samples. Reaction condition: 1.0 mg photocalysts, 0.2 mL $H_2O$ and 10 hours light irradiation.

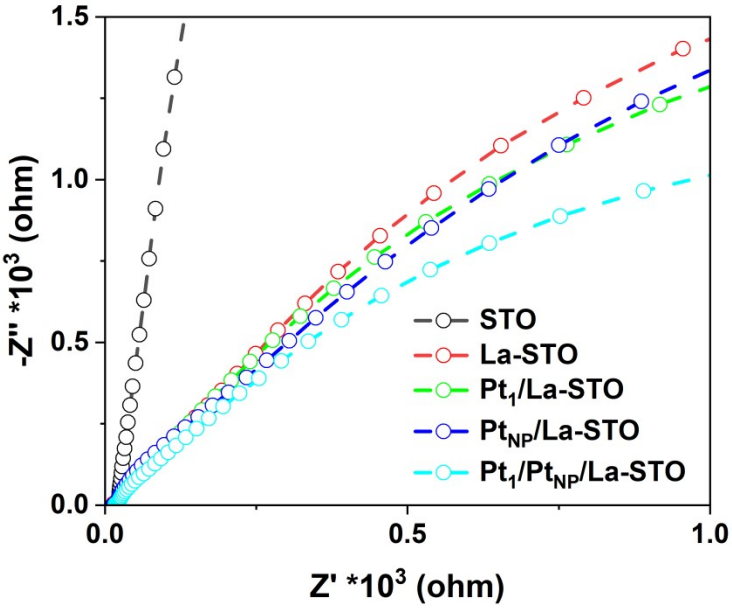


**Fig. S32.** Electrochemical impedance spectroscopy of samples.

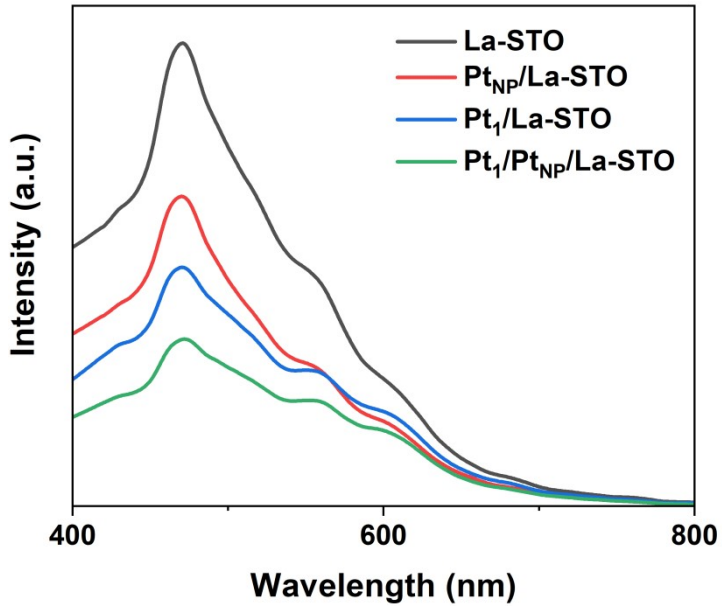


**Fig. S33.** Photoluminescence (PL) emission spectra of different samples.

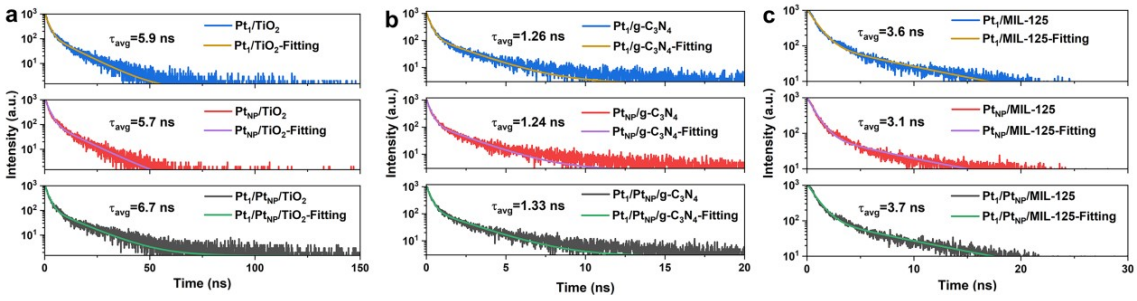


**Fig. S34.** The lifetime of charge carriers over $Pt_1/Pt_{NP}/TiO_2$, $Pt_1/Pt_{NP}/g\text{-}C_3N_4$, $Pt_1/Pt_{NP}$/MIL-125 and the corresponding samples.

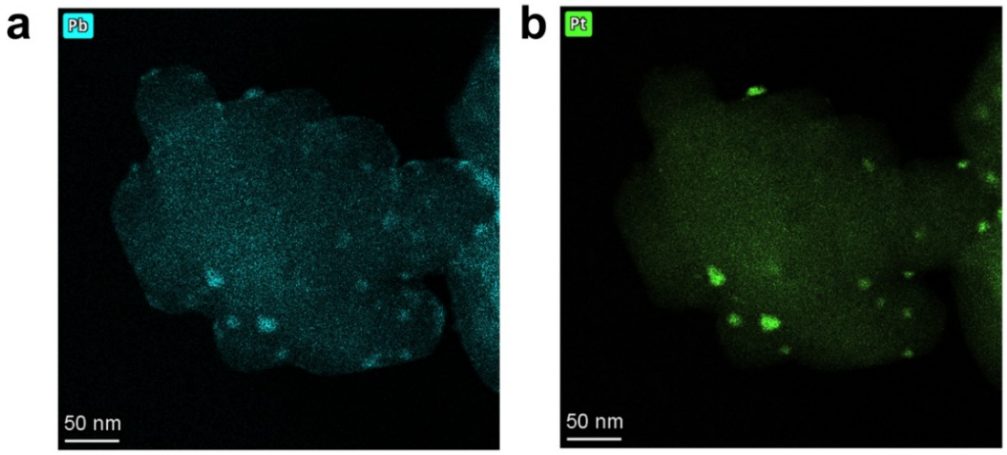


**Fig. S35.** The photo-deposition of $PbO_2$ method was used as probe experiment to demonstrate the location of photo-generated holes during light irradiation. The mapping images of (a) Pb and (b) Pt on $Pt_1/Pt_{NP}$/La-STO.

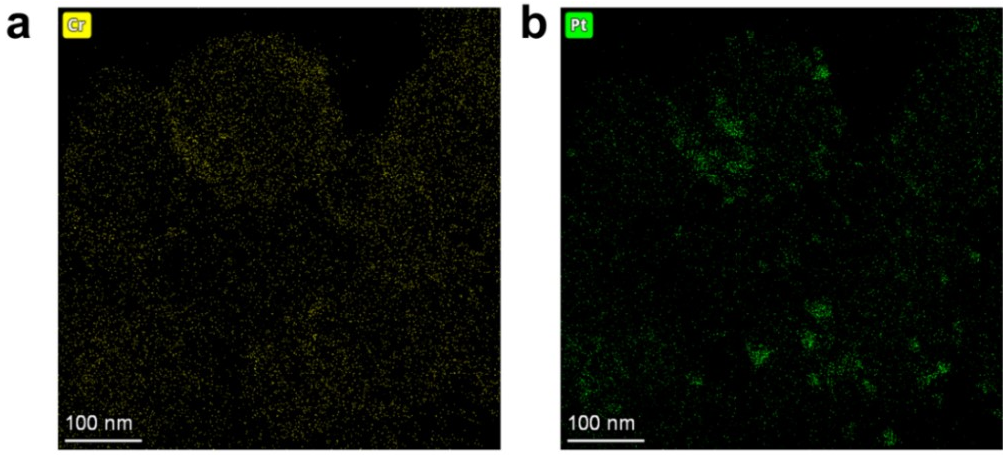


**Fig. S36.** The photo-deposition of $Cr_2O_3$ method was used as probe experiment to demonstrate the location of photo-generated electrons during light irradiation. The mapping images of (a) Cr and (b) Pt on $Pt_1/Pt_{NP}$/La-STO.

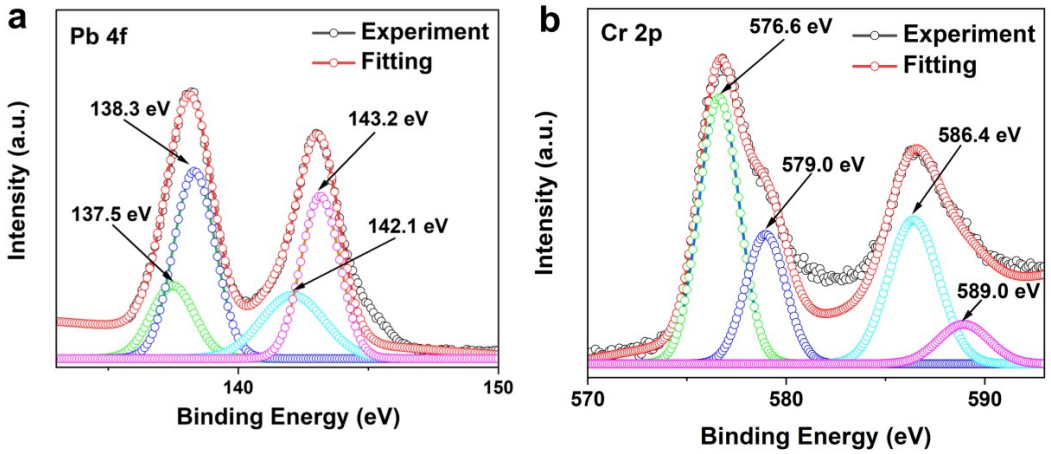


**Fig. S37.** The XPS results of (a) Pb 4f and (b) Cr 2p on the surface of $Pt_1/Pt_{NP}$/La-STO after photo-deposition of $PbO_2$ and $Cr_2O_3$. As for the Pb 4f, the binding energies of 138.3 and 143.2 eV can be assigned to Pb $4f_{7/2}$ and Pb $4f_{5/2}$ of $PbO_2$, respectively. The $Pb^{2+}$ species can be oxidized to $Pb^{4+}$ ($PbO_2$) by the photo-generated holes. The peaks of 137.5 and 142.1 eV are the Pb $4f_{7/2}$ and Pb $4f_{5/2}$ typical binding energies of $Pb^{2+}$, which represent the possible adsorptive $Pb^{2+}$ on the surface of $Pt_1/Pt_{NP}$/La-STO. As for the Cr 2p, the peaks located at about 576.6 and 586.4 eV are the typical binding energies of $Cr^{3+}$ in $Cr_2O_3$. The binding energies of 579.0 and 589.0 eV can be assigned to the typical peaks of $Cr^{6+}$ in $K_2CrO_4$, which due to the possible adsorptive $CrO_4^{2-}$ on $Pt_1/Pt_{NP}$/La-STO surface after the photo-deposition reaction.

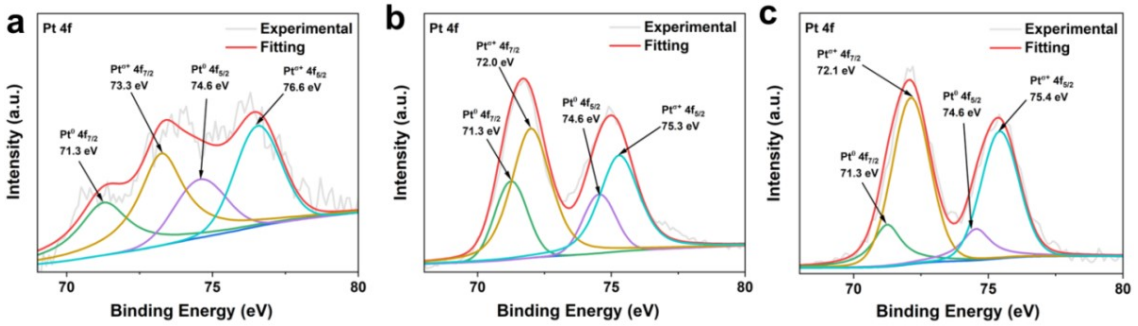


**Fig. S38.** The *quasi-in-situ* XPS measurements of (a) $Pt_1/Pt_{NP}/TiO_2$, (b) $Pt_1/Pt_{NP}$/MIL-125, (c) $Pt_1/Pt_{NP}$/g-$C_3N_4$ after light irradiation.

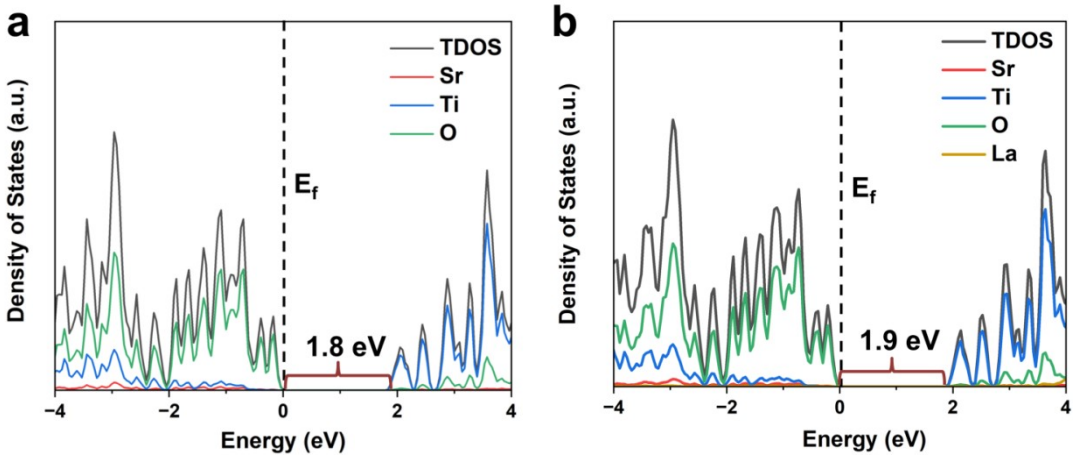


**Fig. S39.** Calculated TDOS and PDOS upon STO and La-STO.

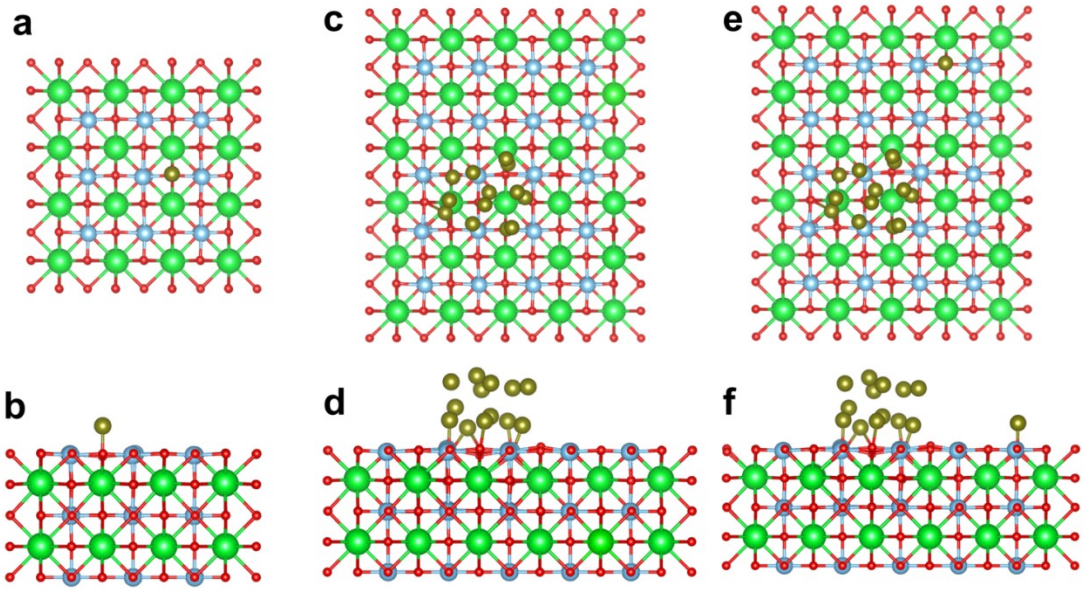


**Fig. S40.** The optimized structural models of $Pt_1$/La-STO (a): top view, (b): side view; $Pt_{NP}$/La-STO (c): top view, (d): side view; $Pt_1/Pt_{NP}$/La-STO (e): top view, (f): side view. The green, blue, red and brown balls are represented as Sr, Ti, O and Pt atoms, respectively.

**Table S1**. Structural parameters extracted from the Pt $L_3$-edge EXAFS fitting. ($S_0^2$=0.81).

| Sample | Scattering pair | CN | R(Å) | $\sigma^2(10^{-3}Å^2)$ | $\Delta E_0$(eV) | R factor |
|---|---|---|---|---|---|---|
| **Pt foil** | **Pt-Pt** | **12*** | **2.76** | **4.4** | **6.8** | **0.002** |
| **$Pt_1$/La-STO** | **Pt-O** | **1.66** | **1.98** | **2.8** | **2.3** | **0.008** |
| **$Pt_1/Pt_{NP}$/La-STO** | **Pt-O** | **1.37** | **2.02** | **2.4** | **10.4** | **0.010** |
| | **Pt-Pt** | **5.80** | **2.75** | **3.9** | **4.5** | |

$S_0^2$ is the amplitude reduction factor; CN is the coordination number; R is interatomic distance (the bond length between central atoms and surrounding coordination atoms); $\sigma^2$ is Debye-Waller factor (a measure of thermal and static disorder in absorber-scatterer distances); $\Delta E_0$ is edge-energy shift (the difference between the zero kinetic energy value of the sample and that of the theoretical model). R factor is used to value the goodness of the fitting.

* This value was fixed during EXAFS fitting, based on the known structure.

Error bounds that characterize the structural parameters obtained by EXAFS spectroscopy were estimated as N ± 20%; R ± 1%; $\sigma^2$ ± 25%; $\Delta E_0$ ± 10%.

$Pt_1/Pt_{NP}$/La-STO (FT range: 2.0-12.0 $Å^{-1}$; fitting range: 1.3-3.3 Å).

$Pt_1$/La-STO (FT range: 2.0-8.0 $Å^{-1}$; fitting range: 1.0-3.0 Å).

Pt foil (FT range: 3.0-12.0 $Å^{-1}$; fitting range: 1-3 Å).

**Table S2.** Comparison the catalytic activity of $Pt_1/Pt_{NP}$/La-STO to recent reported photocatalysts for OWS without sacrificial agents or photosensitizer. Reaction substrate: $H_2O$. The unit of OWS performance has been unified into μmol $g^{-1}$ $h^{-1}$.

| | Samples | Cocatalysts | $H_2$ (μmol $g^{-1}$ $h^{-1}$) | $O_2$ (μmol $g^{-1}$ $h^{-1}$) | Stability | Reference |
|---|---|---|---|---|---|---|
| | $Pt_1/Pt_{NP}$/La-STO | $Pt_1$, $Pt_{NP}$ | 1329.0 | 652.1 | 10 cycles, ≥100 h | This work |
| 1 | Pt@$NH_2$-UiO-66@$MnO_x$ | Pt, $MnO_x$ | 19.6 | 10.1 | 6 cycles, 18 h | Adv. Mater. 2020, 32, 2004747 |
| 2 | $BiVO_4$-FTO | Rh, $Cr_2O_3$, $MnO_x$ | 65.7 | 32.6 | 3 cycle, 12 h | Adv. Sci. 2022, 9, 2105299 |
| 3 | Pt@TpBpy-NS | Pt | 132 | 64 | 5 cycles, 25 h | Nat. Commun. 2023, 14, 593 |
| 4 | $SrTaO_2N$ | $CrO_y$, Ru, $IrO_{2(MW)}$ | 60.67 | 20 | 6 cycles, 18 h | J. Am. Chem. Soc. 2023, 145, 3839−3843 |
| 5 | PCN/LaOCl-2 | Pt, $CoO_X$ | 446 | 214 | 5 cycles, 25 h | Angew. Chem. Int. Ed. 2020, 59, 20919–20923 |
| 6 | Zr-TaON/$Ta_3N_5$ (3 h) | Ru, $Cr_2O_3$, $IrO_2$ | ≈97.2 | ≈44.4 | 2 cycles, 24 h | Angew. Chem. Int. Ed. 2022, 61, e202116573 |
| 7 | TJU-16-$Rh_{0.22}$ | Rh | 31 | 15 | 5 cycles, 15 h | Nat. Catal. 2020, 3, 1027–1033 |
| 8 | Pt@$ZnTiO_{3-x}N_y$@$RhO_x$ | Pt, $RhO_x$ | ≈170 | ≈78 | 3 cycles, 6 h | Small 2021, 17, 2100084 |
| 9 | I-TST | Pt, $Co(OH)_2$ | ≈125 | ≈18 | 1 cycles, 10 h | J. Am. Chem. Soc. 2020, 142, 4508−4516 |
| 10 | g-$C_3N_4$/rGO/PDIP | Pt, $Co(OH)_2$ | 632 | 312 | 21 cycles, 126 h | Adv. Mater. 2021, 33, 2007479 |
| 11 | CNN/BDCNN | Pt, $Co(OH)_2$ | 626.9 | 311.2 | 4 cycles, 24 h | Nat. Energy 2021, 6, 388–397 |
| 12 | $KTaO_3/Ta_3N_5$ | $Rh/Cr_2O_3$ | 36.67 | 18.33 | 3 cycles, 15 h | Nat. Catal. 2018, 1, 756–763 |
| 13 | IEF-11 | Pt | 29.91 | 13.73 | 10 cycles, 240 h | Adv. Mater. 2021, 33, 2106627 |
| 14 | CTF-HUST-A1-$^t$BuOK | $NiP_x$, Pt | 25.4 | 12.9 | 5 cycles, 25 h | Angew. Chem. Int. Ed. 2020, 59, 6007–6014 |
| 15 | r-CTF NSs | Pt | 102.6 | 50.6 | 5 cycles, 25 h | Angew. Chem. Int. Ed. 2021, 60, 25381–25390 |
| 16 | $PbTiO_3/Rh/Cr_2O_3$ | Rh, $Cr_2O_3$ | 32.9 | 17.4 | 1 cycles, 5 h | J. Am. Chem. Soc. 2022, 144, 20342−20350 |
| 17 | $Y_2Ti_2O_5S_2$ | Rh, $Cr_2O_3$, $IrO_2$ | ≈31.25 | ≈15.0 | 2 cycles, 20 h | Nat. Mater. 2019 18, 827–832 |
| 18 | PA-$Ni_{1.1}$@PCN/$Pt_{5hNIR}$ | Pt | 0.058 | 0.027 | 5 cycles, 120 h | Angew. Chem. Int. Ed. 2022, 61, e202212234 |
| 19 | $IrO_2/Bi_2CrO_6$: Ru/$SrTiO_3$:Rh | $IrO_2$, Pt | ≈5.67 | ≈4.38 | 3 cycles, 24 h | Adv. Mater. 2023, 35, 2211182 |
| 20 | 5$Al_2O_3$/Rh/GaN–ZnO | $Al_2O_3$, Rh | ≈906 | ≈480 | 6 cycles, 9 h | Nat. Catal. 2023, 6, 80–88 |